On the accuracy of temperature estimates from in operando X-ray diffraction measurements during additive manufacturing

Steve Gaudez, Daniel Weisz-Patrault, Kouider Abdellah Abdesselam, Hakim Gharbi, Veijo Honkimäki, Steven van Petegem, Manas Vijay Upadhyay

On the accuracy of temperature estimates from *in operando* X-ray diffraction measurements during additive manufacturing

S. Gaudez[1,†], D. Weisz-Patrault[1,**], K. A. Abdesselam[1], H. Gharbi[1], V. Honkimäki[2], S. Van Petegem[3], M.V. Upadhyay[1,*]

[1] Laboratoire de Mécanique des Solides (LMS), École Polytechnique, Institut Polytechnique de Paris, CNRS UMR 7649, 91120 Palaiseau, France
[2] European Synchrotron Research Facility, Grenoble, France
[3] Structure and Mechanics of Advanced Materials, Paul Scherrer Institut, Forschungsstrasse 111, 5232 Villigen PSI, Switzerland

† Current address: Structure and Mechanics of Advanced Materials, Paul Scherrer Institut, Forschungsstrasse 111, 5232 Villigen PSI, Switzerland

* First corresponding author e-mail: manas.upadhyay@polytechnique.edu
** Second corresponding author e-mail: daniel.weisz-patrault@cnrs.fr

Abstract Lattice strains obtained from *in operando* synchrotron X-ray diffraction measurements during metal additive manufacturing are being increasingly used to deduce temperature and cooling rates occurring during the process. The underlying assumption behind this deduction is that lattice strain evolution occurs solely due to temperature changes caused by the passage of the heat-source. However, this assumption crucially neglects the role of mechanical constraints on the sample and the evolution of internal stresses generated due to microstructure evolution. The ensuing elastic strains can have a significant contribution to lattice strains and failure to decouple them from the contribution of thermal strains may induce significant errors in temperature and cooling rate estimates. In this study, we quantify these errors using a combined experimental and numerical approach. First, lattice strains are obtained from *in operando* synchrotron X-ray diffraction measurements during additive manufacturing of a 316L stainless steel thin-wall. Then, the contributions of elastic and thermal strains to the lattice strain are deconvoluted using experimentally validated fast large-scale thermomechanical simulations of the entire AM process. Results reveal that even in the simple case of AM of a single-phase material such as 316L and a thin-wall geometry, significant errors in both temperature amplitudes (up to 30%) and cooling rates (up to 27%) occur when the contribution of elastic strains is neglected. Furthermore, mechanical and thermal effects cannot be trivially decoupled from X-ray diffraction data; fast large-scale thermomechanical simulations become necessary to perform this decoupling.

Keywords 3D printing; synchrotron; lattice strain; thermomechanical modelling; direct energy deposition; residual stress

1 Introduction

Metal additive manufacturing (AM) involves complex interactions between a heat source and feedstock. The ensuing temperature amplitudes, gradients, and heating and cooling rates determine the nature of the different non-equilibrium processes occurring during AM, which in turn determine the material microstructure, its properties, and the eventual part performance. Thus, arguably, temperature is the most important state variable during any metal AM process and its accurate measurement is vital not only to understand the AM process-microstructure-property-performance relationship but also to control it.

Due to the rapid nature of AM, probing temperature *in operando* is very challenging and only a handful of techniques are capable of providing this information. The most common approach that has been used during both directed energy deposition (DED) and powder-bed fusion (PBF) type AM processes involves direct measurements using infrared pyrometers and/or cameras [1–5]. The main difficulty of this technique is the calibration of the emissivity that depends on temperature, surface roughness, etc. However, bi-chromatic technologies enable to mitigate this disadvantage and to obtain quantitative results.

Temperature has also been estimated indirectly from lattice parameters obtained from *in operando* synchrotron X-ray diffraction measurements [6–11]. The main advantages of this approach over infrared techniques include the ability to carry out measurements at a very fine length scale (i.e., distinguish family of grains sharing the same crystallographic orientation), and to directly measure the residual elastic strain after the part cools down to room temperature. The main disadvantage of *in operando* measurements is the nontrivial coupling of all the physical phenomena influencing the lattice parameters, e.g., thermal expansion, elastic strains, solid-state phase transformations, etc. In practice, however, the contributions of elastic strains and solid-state phase transformations are neglected in order to obtain a temperature estimate from the lattice parameter. This approximation can introduce significant errors in temperature and cooling rate estimates. The problem can be simplified by studying single-phase materials or using an experimental setup allowing to probe a nearly strain-free direction or both. For example, in an *in operando* synchrotron diffraction experiment during laser PBF of a single-phase nickel alloy, it was briefly shown that elastic strains on the top surface normal to the building direction were small and could be ignored to estimate temperature [11].

In this work, an in-depth analysis is conducted to quantify the contribution of both elastic and thermal strains to the lattice strains and study the impact of neglecting elastic strains on temperature and cooling rate estimates. To facilitate this analysis, the material studied is a 316L stainless steel, which remains mostly austenitic so that solid-state phase transformations can be neglected. The following combined experimental and numerical simulation-based sequential procedure is followed: (i) *in operando* synchrotron X-ray diffraction experiments are performed during AM of thin-wall shaped 316L samples using a dedicated miniature laser-based DED machine [12], (ii) thermomechanical simulations of the entire DED process are performed using a recently developed fast large-scale numerical model [13], (iii) model assumptions are validated by comparing simulation results with measurements for both the final residual elastic strain distribution and transient thermal + elastic strain during fabrication, and (iv) the errors induced in neglecting the contribution of elastic strains on temperature and cooling rate estimates are quantified and the difficulty of decoupling mechanical and thermal contributions only from X-ray diffraction measurements is made apparent.

The paper is organized as follows. Materials and methods are detailed in Section 2, and

the fast large-scale thermomechanical model is briefly recalled in Section 3. Experimental and numerical results are presented and compared in Section 4. Finally, the effect of neglecting elastic strains when estimating temperature and cooling rates from lattice strains measured during *in operando* synchrotron X-ray experiments is discussed in Section 5 and concluding remarks are provided in Section 6.

2 Materials and methods

2.1 Material and printing strategy

AM of 316L stainless steel was performed using a miniature laser metal deposition (mini-LMD) machine designed to perform *in situ* and *in operando* synchrotron X-ray experiments; a detailed description of the machine can be found in [12]. The feedstock was a 316L powder (Oerlikon AM, Germany) manufactured via inert gas atomization. The average powder particles size was 58 µm with 10% and 90% quantiles being 44 µm and 82 µm, respectively. The chemical composition of the powder in weight percent is reported in Table 1.

Table 1: Chemical composition of the 316L powder in weight percent.

Fe	Cr	Ni	Mo	Mn	Si	N	Cu	O	P	S	C
Bal.	17.34	12.55	2.34	1.40	0.49	0.08	0.04	0.03	0.1	<0.1	<0.1

100-layered thin-wall shaped samples of size $0.6 \times 100 \times 20$ mm^3 (x, y, z) were additively manufactured with the mini-LMD machine using a single-pass-per-layer unidirectional printing strategy. The printing direction (PD) was along y and the building direction (BD) along z. Each wall was printed on a 316L substrate of size $40 \times 140 \times 10$ mm^3, 5 mm away from the edge along the transverse direction (TD) x, and centered along the PD y. The following AM parameters were used: laser power = 105 W, printing speed = 10 mm.s^{-1}, powder flow rate = 7 g.min^{-1}, and a mean layer height of 0.2 mm. A dwell time of 14 s was set between the end of a printed layer and the beginning of the next one; this dwell time is the minimum time required to allow the experimental setup to be ready to print the next layer and for the X-ray detector to prepare for the next series of acquisitions. Thus, a full cycle to print one layer took 24 s (10 s of printing + 14 s of dwell time). AM was performed by keeping the printing head (powder and laser) static and by moving the substrate holder along PD (y) with respect to the mini-LMD machine.

2.2 Synchrotron experiments

In operando synchrotron X-ray diffraction experiments during AM were conducted at the European Synchrotron Radiation Facility (ESRF, France) on beamline ID31. The mini-LMD machine was positioned on the heavy duty micro diffraction instrument (HDMD) available at the beamline. A 77 keV ($\lambda = 0.16102$ Å) X-ray beam of size 300×300 µm^2 (obtained with slits) was used. A Pilatus 3X CdTe 2M 2D detector (pixel array of 1475×1679 (y, z) and pixel size of 172×172 µm^2) located at ∼0.8 m downstream to the sample was used to record the diffraction patterns with an acquisition frequency of 20 Hz. Thus, 200 images were recorded for each printed layer. With this setup, full Debye-Scherrer rings of the first four *hkl* reflections of the γ-austenite (fcc) phase of 316L were investigated, i.e., 111, 200, 220, and 311. Sample-to-detector

distance, detector tilts, and beam center were calibrated using a CeO_2 powder as a reference. The experimental setup and the coordinate system used, are presented in Figure 1a.

For each experiment, the vertical distance (z) between the top of the substrate and the center of the X-ray beam was kept fixed in order to investigate the material at a fixed height on the wall. Three experiments were conducted to measure at three vertical distances (z): 4 mm (20th layer), 7.4 mm (37th layer), and 11 mm (55th layer). Then, the walls were manufactured up to a total of 100 layers ($\sim$ 20 mm) and diffraction patterns were recorded during the addition of each layer. Since the printing head is kept stationary with respect to the mini-LMD machine, the substrate holder is moved down ($-z$) by a layer increment (0.2 mm) after the addition of a layer and prior to printing the next one. At the same time, in order to maintain the same vertical distance between the substrate and the X-ray beam, the mini-LMD machine is moved up ($+z$) by a layer increment (0.2 mm) using the HDMD instrument. In addition, during the printing of a single layer, in order to continuously investigate multiple locations ahead of the laser as well as behind it, the mini-LMD machine was moved in the direction opposite to the PD using the HDMD at a speed of 4 mm.s^{-1} during deposition of a layer (10 s) (Figure 1b). After the deposition, the machine was moved back to its original position during the dwell time.

During the deposition of a layer, the detector was synchronized to start acquiring images when the laser was turned on and to stop acquiring when the laser was turned off. At the start of the printing of the layer when the laser was just turned on, the X-ray beam was 20 mm ahead of the laser (Fig. 1b). At the end of the printing of that layer, the X-ray beam was 20 mm behind the laser (Fig. 1b). Therefore, from the point of view of the laser, images were acquired in the range $\pm$20 mm around the laser along PD (y) i.e., along a 40 mm distance (d_{l-X}).

Now, with respect to the sample, images were acquired over a length of 60 mm at $\pm$30 mm along y from the center of the sample during a period of 10 s; substrate holder speed ($v_{substrate}$) of 10 mm.s^{-1} along $-y$ and HDMD speed of 4 mm.s^{-1} along y result in a relative speed of 6 mm.s^{-1} of the X-ray beam with respect to the sample, which requires 10 s to cover the distance of 60 mm. Since 200 images are taken using a 300 $\times$ 300 µm^2 (y, z) beam, the probed volume per image is 0.6 $\times$ 0.6 $\times$ 0.3 mm^3 (x, y, z).

A reference laser time scale (t_{ref}) is used instead of the distance scale to simplify data representation and interpretation (see Figure 1c). This scale is constructed based on the following considerations. In the reference frame of the sample, at any given instant, irrespective of the location probed by the X-rays, the laser is either approaching or moving away from that location at a constant speed of 10 mm/s. Now, as mentioned earlier, with respect to the laser, the X-rays are probing a distance of $\pm$20 mm around the laser. Therefore, the reference time scale is $t_{ref} = d_{l-X}/v_{substrate} = 4$ s. In order to better understand this scale, consider a thought experiment where the substrate and HDMD are kept immobile with respect to the laboratory frame and the focusing head is moving at a speed of 10 mm/s. The thought experiment and the present experiment will result in the same printing conditions for the sample and the same time t_{ref} to probe the locations within a distance of $\pm$20 mm with respect to the laser.

The acquired 2D diffraction patterns (Debye-Scherrer rings) were integrated azimuthally, with a code available at the beamline, into 36 cakes of 10° each taking into account the detector thickness to obtain 36 different I vs. 2θ line profiles. Single peak fitting was performed for each of the hkl peaks using a Pearson VII function combined with a linear function for the background to obtain the average position of each peak. In addition, azimuthal integration was also performed on the full Debye-Scherrer rings i.e., over the 360° angular range, for data

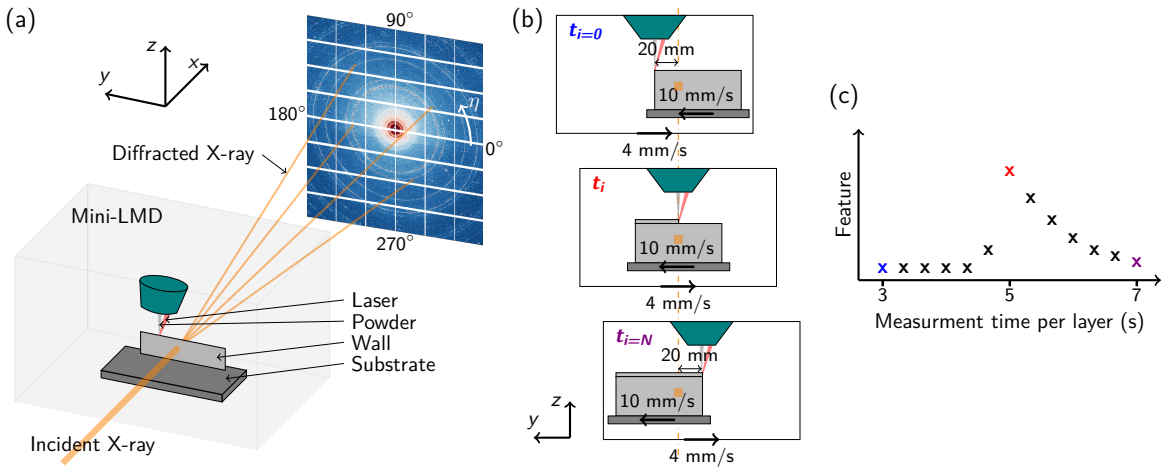

Figure 1: (a) Experimental setup used during the *in operando* synchrotron experiments. (b) Printing strategy used during one layer addition from the point of view of the X-ray beam. (c) Resulting data in the reference laser time scale. The orange square in (b) represents the X-ray beam position.

representation in Figure 4b.

Lattice strains were calculated from the change in the average peak positions of each of the hkl peaks using:

$$\varepsilon^{hkl} = \frac{\sin\theta_0^{hkl}}{\sin\theta^{hkl}} - 1 = \frac{d^{hkl} - d_0^{hkl}}{d_0^{hkl}} \tag{1}$$

where ε^{hkl} is the lattice strain, θ_0^{hkl} is half of the strain-free diffraction angle, θ^{hkl} is half of the measured diffraction angle, d_0^{hkl} is the strain-free interplanar spacing, and d^{hkl} is the measured interplanar spacing distance of a given $\{hkl\}$ plane family. The strain-free lattice parameter was obtained from measurements of a matchstick-shaped sample extracted from the material printed with the same AM parameters. For the material investigated, the mean strain-free lattice parameter obtained from the four aforementioned reflections is $a_0 = 3.59730 \pm 0.00026$ Å. The arithmetic mean strain (ε^{lat}) of the 111, 200, 220, and 311 reflections is used in this work. This choice was validated by comparing the average elastic strain against the elastic strain from the 311 reflection for the experimental residual strain maps presented in Figure 3. The difference between the two elastic strains, $\varepsilon^{\text{e}}_{311}$ and $\varepsilon^{\text{e}}_{\text{average}}$, is in the range of $\pm 0.025\%$. The latter estimate is used in this work to facilitate comparison with the simulated elastic strain.

The evolution of lattice strains along the horizontal ($\varepsilon^{\text{lat}}_{yy}$) and the vertical ($\varepsilon^{\text{lat}}_{zz}$) directions in the sample were evaluated from two $\pm 10°$ cakes with respect to the horizontal y (PD corresponding to 0° and 180° azimuthal angles) and the vertical z (BD corresponding to 90° and 270° azimuthal angles) directions (see Figure 1a for the convention).

2.3 Electron back-scattered diffraction (EBSD) investigation

EBSD measurements were carried out in a FEI quanta 650 FEG scanning electron microscope equipped with a Symmetry detector (Oxford Instruments) to investigate the microstructure, the grain size, morphology, and orientation in the $y-z$ plane of the as-built sample (see Figure 1a). EBSD investigation was performed on a section of the sample extracted from the middle (along y) of the substrate and the as-built wall. This section was ground with abrasive paper up to 4000

grit, then using 1 µm diamond paste, followed by 50% diluted OPA solution, and finally etched using 10% oxalic acid for 10 s at 5 V. The EBSD acquisition was performed at 30 keV with a step size of 1.5 µm and an acquisition time of 0.6 ms. Each acquired image has a resolution of 750×500 µm^2. An overlap of 10% in each direction was used to reconstruct the full EBSD map. The maps were analyzed using the AZtec 6.0 SP1 software considering two phases: α ferrite (bcc) and γ austenite (fcc). Pixel confidence index before data post-processing was greater than 97.5%. Post-processing was done with the AZtec Crystal 3.0 software to facilitate visualization.

3 Numerical analysis

The numerical simulation of the entire process relies on (i) a thermal analysis [3,14], and (ii) a finite element analysis (FEA) of the mechanics of the problem based on shell elements [5]. The thermomechanical model is weakly coupled in the sense that the effect of mechanics (i.e., elastic and plastic deformation) is neglected in the temperature calculation. This assumption is acceptable because both elastic and plastic distortions are sufficiently small such that mechanical dissipation plays a negligible role in changing temperature in comparison to the heat added by the laser. The simulation procedure is as follows: the temperature field history is first computed during the building of the entire part. The computed thermal strains are then introduced as eigenstrains in the mechanical model to compute the stresses and distortions. The detailed description and key assumptions of the model can be found in [3,5]. Below, only the governing equations, input parameters and boundary conditions of the weakly coupled thermomechanical model are briefly recalled.

The thermal part of the model assumes that liquid metal is directly deposited at a temperature T_{dep} that is higher than the liquidus and computed as [15]:

$$T_{\text{dep}} = \frac{I\,\eta\,R_{\text{beam}}}{\sqrt{2\pi}\lambda_{\text{liq}}} \arctan\left(\frac{\sqrt{8\,D_{\text{liq}}t_{\text{beam}}}}{R_{\text{beam}}}\right) \tag{2}$$

where R_{beam} is the laser spot radius defined as two standard deviations of the Gaussian laser distribution, λ_{liq} and D_{liq} are respectively the thermal conductivity and diffusivity of the liquid metal, $I = 2\,P_{\text{beam}}/(\pi R_{\text{beam}}^2)$ is the laser intensity, η is the absorptivity of the powder, and $t_{\text{beam}} = \sqrt{2}\,R_{\text{beam}}/V_{\text{beam}}$ with V_{beam} being the laser beam velocity. Boundary conditions include convection at the bottom of the sample to mimic heat conducted to the substrate, heat loss by convection on the other surfaces due to surrounding gas and by radiation, and the heat extracted by the cover/shielding gas. The cover gas effect has been modeled by directly imposing a volumetric heat loss that is extracted by the cover gas according to a Gaussian moving distribution [3]:

$$Q_{\text{gas}}(t) = 2\frac{H_{\text{gas}}}{h_x}(T - T_{\text{amb}}) \exp\left(-2V_{\text{beam}}^2 \frac{(t - t_n)^2}{R_{\text{gas}}^2}\right) \tag{3}$$

where T_{amb} is the ambient temperature, H_{gas} is the heat transfer coefficient (HTC) associated with the gas flow, R_{gas} characterizes the area affected by the gas flow, and h_x is the thickness of a bead (smallest portion of a modeled layer).

In addition, latent heat of fusion is taken into account during solidification. Some proportion η of the power is used to melt the powder, which is already taken into account in Equation (2), and some proportion η_{beam} may be absorbed by the layer on top of which the deposition is made. Assuming a Gaussian laser spot, the associated power per unit volume absorbed by the

top layer is [3]:

$$Q_{\text{beam}}(t) = \frac{2\eta_{\text{beam}} P_{\text{beam}}}{\pi h_z R_{\text{beam}}^2} \exp\left(-2V_{\text{beam}}^2 \frac{(t-t_n)^2}{R_{\text{beam}}^2}\right) \tag{4}$$

where h_z is the bead height, and t_n is the time of metal deposition for the considered 2D multilayer structure. It should be noted that the contribution of Equation (4) was not very high in [3,5,14] as the laser was coaxial with the nozzle spraying the powder. But in this study, the laser is tilted with respect to the spraying nozzle [12] so that a significant proportion of the laser is directly absorbed by the existing layer on top of which the metal deposition is made.

The mechanical part of the model [5] combines element birth and element activation techniques. The former progressively adds new elements to the existing mesh, while the latter involves using a single unchanging mesh of the part with very low stiffness and progressively assigning realistic stiffness and material properties to the elements. A hybrid strategy combining element birth and element activation is followed: each new layer is added to the existing mesh (with low stiffness) at the end of the dwell time, and then the real material properties are assigned to the first element (in the direction of lasering) of this new layer when the laser begins printing this new layer. Meanwhile, at each time increment real stiffness is assigned to a single element in the wake of the laser. Since a thin-walled structure is considered, shell elements are used (i.e., 2D Reisner-Mindlin theory). The details of this implementation to compute the Cauchy stress field can be found in [5].

Temperature-dependant elasto-plastic behavior is considered. Material properties are fitted from data at high temperatures obtained in [16] for the yield stress and in [17] for shear and Young's moduli, and at room temperature from data reported in previous studies [18, 19]. A linear temperature dependence is assumed for the Young's ($E(T)$) and shear ($\mu(T)$) moduli:

$$E(T) = E_0\left(1 - \beta_E\left(T - T_0\right)\right) \tag{5}$$

$$\mu(T) = \mu_0\left(1 - \beta_\mu\left(T - T_0\right)\right) \tag{6}$$

where $T_0 = 273.15$ K, E_0 is the Young's modulus at T_0, μ_0 is the shear modulus at T_0, and β_E and β_μ are fitting parameters. Following [20], the thermal expansion coefficient for 316L was assumed to have a quadratic dependence on temperature:

$$\alpha(T) = \alpha_0\left(1 + \beta_\alpha T + \gamma_\alpha T^2\right) \tag{7}$$

where α_0 is a nominal thermal expansion coefficient, and β_α and γ_α are fitting coefficients. The yield stress dependence on temperature is modeled using an exponential rule:

$$\sigma_Y(T) = \sigma_0\left[1 + \beta_Y \exp\left(-\gamma_Y(T - T_0)\right)\right] \tag{8}$$

where σ_0 is the yield stress at high temperature, β_Y is a dimensionless coefficient, and γ_Y is a fitting coefficient. The kinematic hardening coefficient denoted by H_Y is assumed to be a constant. The values of the input parameters of the weakly coupled model are listed in Table 2.

4 Results

4.1 Microstructure characterization

EBSD imaging (Figure 2a) was performed on the as-built microstructure along the $y-z$ plane to obtain information about texture, grain size, and morphology. A 10° misorientation threshold

Table 2: Input parameters.

Number of layers	N_{lay}	(-)	100
Substrate thickness	h_{sub}	(mm)	10
Initial substrate temperature	T^0_{sub}	(K)	300
Length of wall	L	(mm)	100
Layer height	h_z	(µm)	200
Layer thickness	h_x	(µm)	600
Laser beam radius	R_{beam}	(µm)	200
Laser beam speed	V_{beam}	(mm.min^{-1})	600
Laser beam power	P_{beam}	(W)	100
Dwell time	t_{dwell}	(s)	14
Powder absorptivity	η	(-)	0.4
Proportion absorbed by the top layer	η_{beam}	(-)	0.17
Laser beam radius	R_{beam}	(µm)	200
Liquidus temperature	T_{liq}	(K)	1726
Solidus temperature	T_{sol}	(K)	1607
Thermal conductivity of the liquid metal	λ_{liq}	($\text{W.m}^{-1}\text{.K}^{-1}$)	30
Thermal diffusivity of the liquid metal	D_{liq}	($\text{m}^2\text{.s}^{-1}$)	13×10^{-6}
Thermal conductivity of the solid metal	λ_{sol}	($\text{W.m}^{-1}\text{.K}^{-1}$)	21
Thermal diffusivity of the solid metal	D_{sol}	($\text{m}^2\text{.s}^{-1}$)	5.25×10^{-6}
Latent heat of fusion	L_f	(J.mm^{-3})	2.1
HTC part/air	H_{air}	($\text{W.m}^{-2}\text{.K}^{-1}$)	15
HTC part/build platform	H_{build}	($\text{W.m}^{-2}\text{.K}^{-1}$)	20000
HTC part/cover gas	H_{gas}	($\text{W.m}^{-2}\text{.K}^{-1}$)	300
Young modulus at 273.15 K (5)	E_0	(MPa)	192835
Coefficient (5)	β_E	(K^{-1})	4.2×10^{-4}
Shear modulus at 273.15 K (6)	μ_0	(MPa)	77765
Coefficient (6)	β_μ	(K^{-1})	4.3×10^{-4}
Thermal expansion coefficient at 0 K (7)	α_0	(K^{-1})	17.9×10^{-6}
Coefficient (7)	β_α	(K^{-1})	2.714×10^{-4}
Coefficient (7)	γ_α	(K^{-2})	4.046×10^{-8}
Yield stress at high temperature (8)	σ_0	(MPa)	66
Coefficient (8)	β_Y	(-)	4.435
Coefficient (8)	γ_Y	(K^{-1})	2.236×10^{-3}
Hardening coefficient	H_Y	(MPa)	1200

was used to highlight grain boundaries. Along the wall height (z) a fine and homogeneous microstructure is observed with grains having a preferred inclination towards PD. At the bottom of the wall close to the substrate, the grains are more elongated than the ones in the middle and the top, however, their sizes are similar along BD. The grain size in the entire wall was quantified via their observed surface area and a monomodal distribution was obtained. The first quartile, the median, and the third quartile of the grain surface area distribution are respectively 101 µm^2, 268 µm^2, and 700 µm^2 (the corresponding equivalent diameters are 11.3 µm, 18.5 µm,

and 29.9 µm). The {100} pole figure shows a preferred ⟨001⟩ orientation of the grains along the y direction of the wall (Figure 2b). Nevertheless, the observed texture can be considered weak. The two other pole figures show a negligible preferred orientation. These results are confirmed via synchrotron X-ray diffraction by analyzing the peak intensity I_{hkl} evolution as a function of the azimuthal angle η. The microstructure homogeneity and the weak texture observed support the use of large-scale simulation with isotropic material properties.

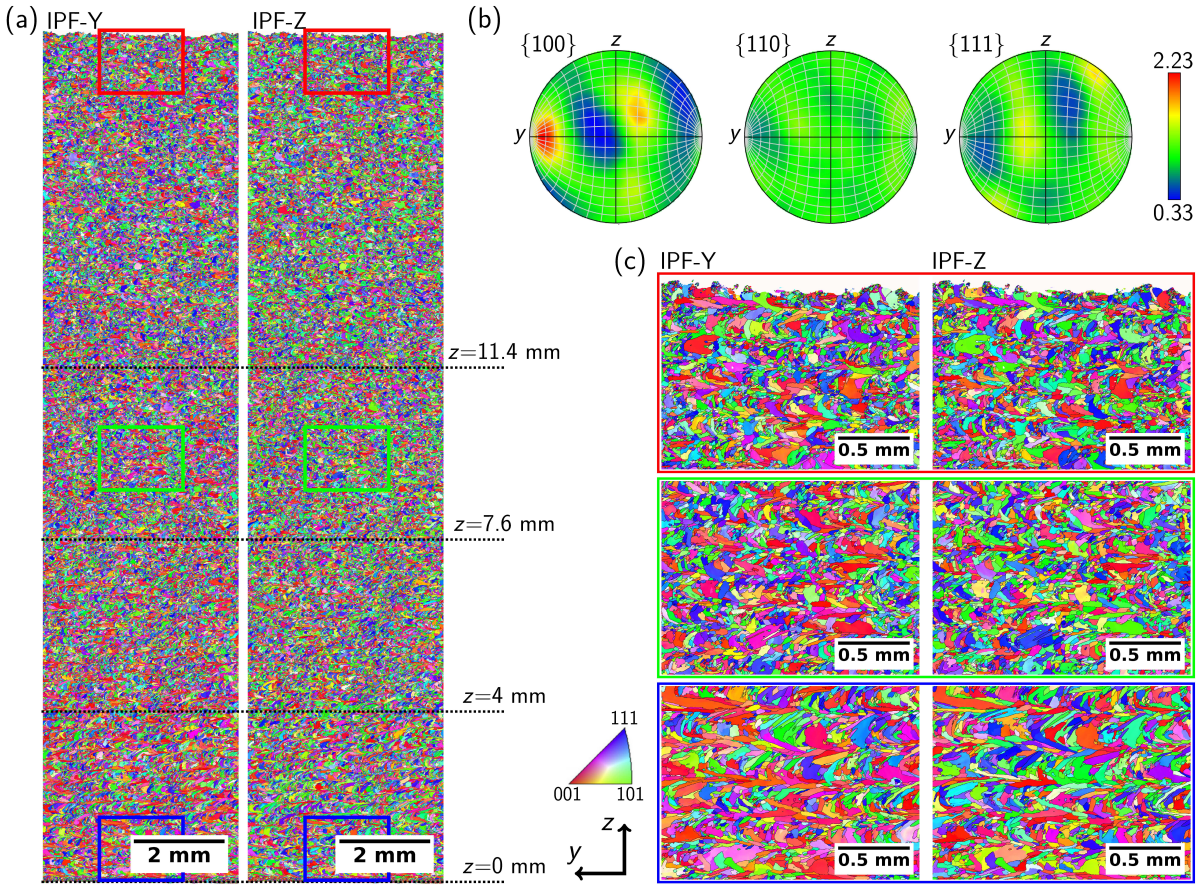

Figure 2: (a) inverse pole figure y (IPF-Y) and z (IPF-Z) orientation maps along the $y-z$ plane obtained via EBSD, (b) the corresponding pole figures, and (c) zoomed IPF-Y and IPF-X EBSD maps from the bottom (blue zone), middle (green zone), and top (red zone) of the wall in (a). The z position of the three regions investigated via *in operando* synchrotron X-ray diffraction are shown in (a). The coordinate axes and IPF color legend are common to (a) and (c).

4.2 Residual elastic strains - measurements and predictions

Following the justification of using isotropic material properties in Section 4.1, simulations of the building of 100-layer walls are performed and the predicted residual elastic strains are compared with those obtained from synchrotron X-ray diffraction measurements. Figure 3a and c show the measured mean residual elastic strain distribution (a) ε^{e}_{yy} and (c) ε^{e}_{zz} within the wall at room temperature at the end of building. Residual strains are non-uniform across the sample, both along the BD and PD, due to the thermomechanical conditions arising during building from the sample geometry, boundary conditions, and heat-matter interactions. Close to the center of the sample, residual strains are tensile along PD and compressive along BD. Along PD, the

highest magnitude occurs in the last few deposited layers; according to a recent study [12], the magnitude is the highest in the 5th layer below the topmost layer. However, at the edges of the wall ($y = -50$ to -40 mm and $y = 40$ to 50 mm) the opposite trends, compression along PD and tension along BD, are observed.

The simulation predicted residual elastic strains are shown in Figure 3b and d. In general, they are in excellent agreement with the experimentally measured ones. At the edges of the sample, some discrepancies are visible between the measured and simulated strains due to the fact that unlike the simulated geometry, the printed thin-walls are not perfectly rectangular. Despite this difference, the Pearson product-moment correlation coefficient between experimental and simulated results is 0.9 for the PD and 0.86 for the BD strains, which consolidates the excellent match and validates a significant part of the model and its assumptions [3,5]. Notably, simulations capture the asymmetry in the elastic strains with respect to $y = 0$ (not evident in the experimental measures because of edge effects) due to the unidirectional printing strategy from $y = -50$ mm to $y = 50$ mm.

On the basis of this match, this model is used to study the effect of elastic strain (ε^e) on the temperature (T) estimated from the measured lattice strain (ε^{lat}). Note that while a good match of the residual lattice strains does not automatically imply a good match of the *in operando* measurements, it nevertheless provides a higher degree of confidence in the simulation predictions. Nevertheless, as shall be seen in Section 4.3), the model predictions are also validated against *in operando* measurements.

4.3 *In operando* synchrotron X-ray diffraction measurements and comparison with simulations

Figure 4 shows some of the diffraction patterns obtained during the addition of the 20$^{\text{th}}$ layer i.e., L_{20} ($z = 4$ mm in Figure 2a); the time $t = 0$ s in Figure 4 and the text below refers to the beginning of the printing of a layer. Focusing first on the 2D diffraction patterns in Figure 4a, at $t = 5.06$ s, an amorphous pattern is observed due to the presence of the liquid phase. Then, at $t = 5.12$ s, the material has solidified and Debye-Scherrer patterns with distinct large spots are observed due to the presence of coarse austenite grains. In addition, Debye Scherrer rings are also observed due to the colder powder illuminated by the X-ray beam as the focusing head passes overhead. Finally, at $t = 5.32$ s, only the Debye-Scherrer rings from the solidified material are visible.

In order to better understand the appearance and disappearance of different phases, the Debye-Scherrer patterns are integrated over the azimuthal angle η to obtain diffraction line profiles I vs. 2θ as a function of time. At $t = 5.06$ s, the diffraction peaks from the powder and from the previously deposited layer are visible; recall that the X-ray beam height is slightly larger than the layer height and it interacts with the layer below. The amorphous pattern, barely visible at $t = 5.12$ s, shows the end of solidification following which the solid phase is mainly austenitic. Just after solidification and until the end of printing of the layer, a faint {101} diffraction peak corresponding to the ferrite phase is obtained, although it is not visible in Figure 4b. Rietveld refinement estimates the ferrite phase fraction to be lower than 0.5 wt%.

Figure 4c shows the processing time vs. 2θ plot for the different profiles for layers L_{20} and $L_{20} + 1$. As the laser approaches the investigated region, all the diffraction peaks shift towards lower 2θ angles because of the temperature increase. The opposite trend is observed after melting and during solidification i.e., all the diffraction peaks shift towards higher 2θ angles because of

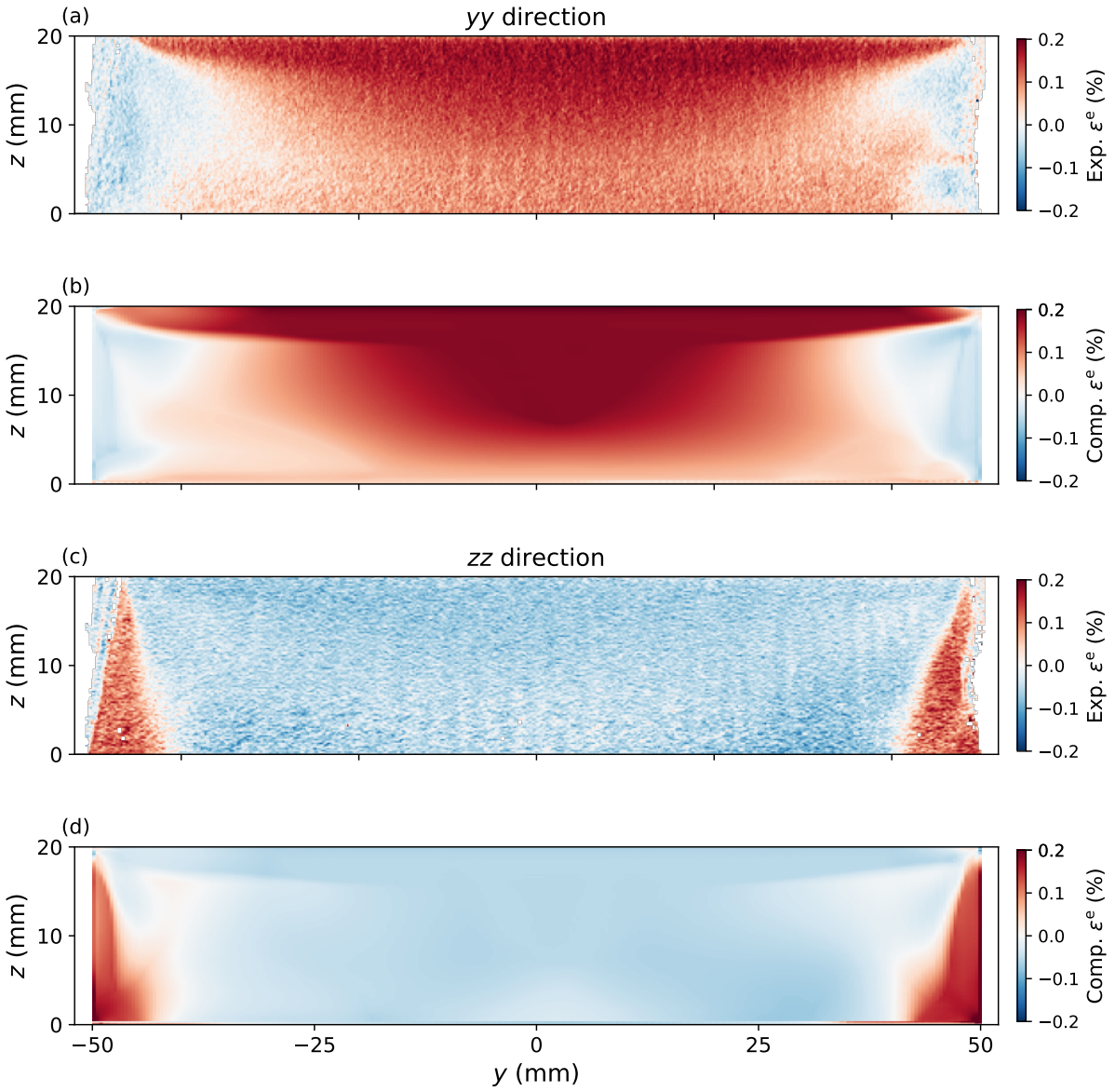

Figure 3: (a, c) Experimental (Exp.) and (b, d) computed (Comp.) residual strain maps at room temperature after the building of 100 layers: (a and c) ε^{e}_{yy} (PD) and (b and d) ε^{e}_{zz} (BD). Experimental measurements were done with a scanning step of 200 µm in both directions, while the mesh is composed of 400 µm × 200 µm elements. The center of the wall was set at y = 0 mm and the top of the substrate at z = 0 mm. Printing started at y = -50 mm and ended at y = 50 mm.

the temperature decrease.

Figure 5 shows the mean lattice strain ε^{lat}_{yy} and ε^{lat}_{zz} evolution due to the intrinsic heat treatment generated during AM as a function of the measurement time per layer for building commencing at layer height z = 4 mm i.e., with the deposition of layer L_{20}.

Focusing first on ε^{lat}_{yy} (Figure 5a), during printing of L_{20}, the signal from t = 3 s to 5 s is coming from the previously printed layer L_{19}. Starting with a slight tensile residual strain, the lattice parameter gradually decreases until t = 5 s. When the molten material is deposited at t = 5 s, it becomes impossible to fit the data because of the absence of diffraction peaks

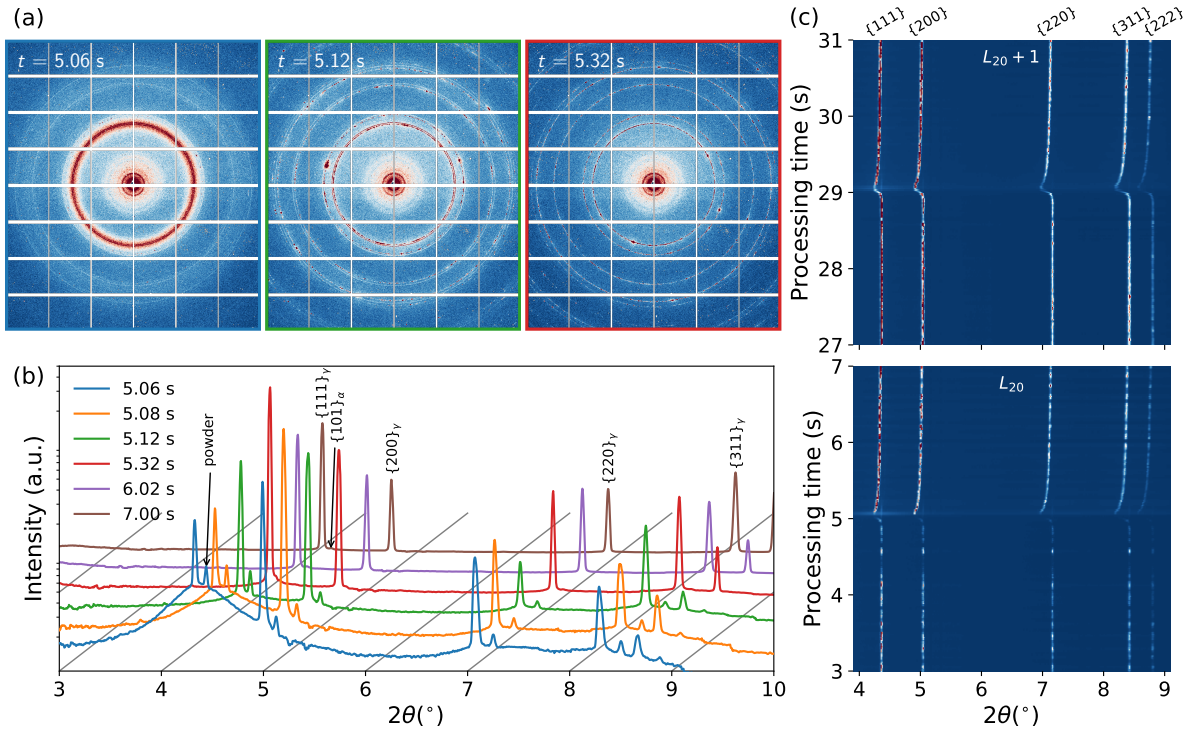

Figure 4: (a) 2D detector images at different processing times during AM of layer L_{20}, (b) evolution of diffraction profiles of layer L_{20} while deposited at different processing times, and (c) stacked diffraction profiles over processing time during the addition of 2 layers, L_{20} and $L_{20}+1$. The colors used to enclose the detector images in (a) correspond to the colors of the diffraction profiles shown in (b).

(amorphous patterns coming from the liquid). Discernible diffraction patterns reappear only after solidification ($t > 5$ s), at which point $\varepsilon_{yy}^{\text{lat}}$ is very high due to thermal expansion and it continuously decreases due to subsequent thermal contraction. After cooling down to room temperature (at $t = 3$ s for layer $L_{20}+1$), the probed volume on layer L_{20} has a residual $\varepsilon_{yy}^{\text{lat}}$ of $\sim 0.18\%$; this result is consistent with our previous study focusing on the {400} plane family of single grains in the bulk [12]. This tensile strain can be explained by the temperature gradient mechanism [21] occurring during local cooling of a single-phase material. Next, during the printing of $L_{20}+1$, as the laser approaches the probed volume, the residual $\varepsilon_{yy}^{\text{lat}}$ shows a continuous decrease until ~ 4.8 s due to a decrease in interplanar spacing. The contraction is gradual from 3 s to ~ 3.8 s, but it steepens after ~ 3.8 s as the laser comes closer to the probed volume. This contraction is the result of the restricted expansion of the heated material by the surrounding cooler material leading to the development of compressive strains [21, 22]; similar contractions have been reported during laser processing of a Ti6Al4V alloy [23], L-PBF AM of Inconel 625 alloy [22], and L-DED AM of high carbon steel [8] via *in operando* synchrotron experiments and predicted with a numerical thermomechanical model for Inconel 718 alloy [24]. After ~ 4.8 s, $\varepsilon_{yy}^{\text{lat}}$ increases due to the heat input caused by the proximity of the laser with the probed volume and then decreases after the passage of the laser ($t > 5$ s), similar to the deposition of L_{20}.

Meanwhile, contrary to $\varepsilon_{yy}^{\text{lat}}$, $\varepsilon_{zz}^{\text{lat}}$ starts with a compressive residual strain at the start of the

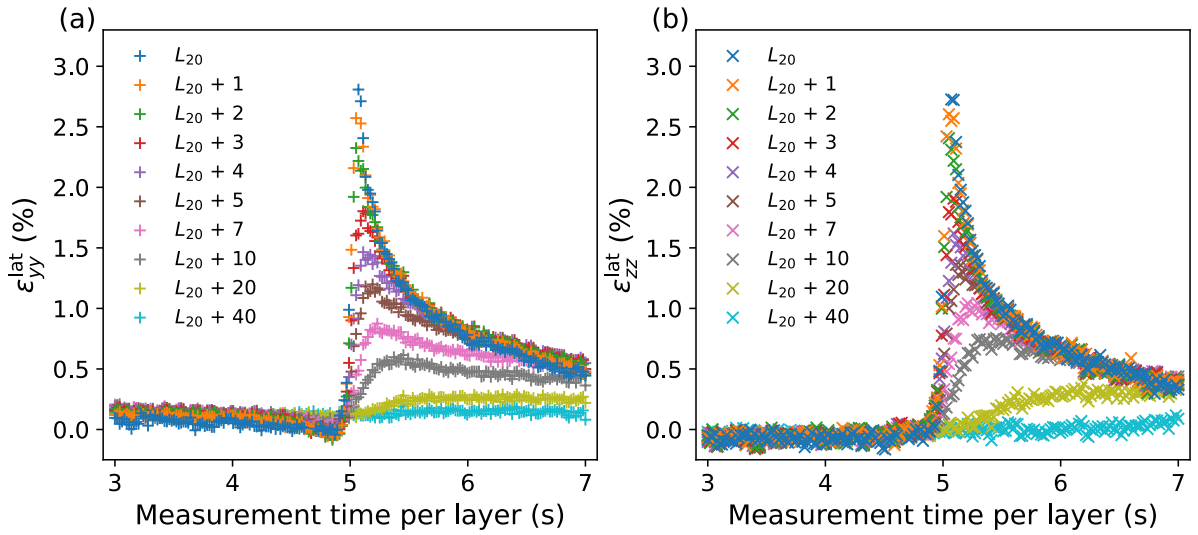

Figure 5: Evolution of (a) ε_{yy}^{lat} (along PD) and (b) ε_{zz}^{lat} (along BD) at $z = 4$ mm above the substrate during the LMD process (see Figure 2 for reference to heights).

deposition of L_{20} (Figure 5b). It slightly increases until the laser approaches very close to the probed region. Then, similar to ε_{yy}^{lat}, ε_{zz}^{lat} increases and the fit is lost due to the presence of a local melt pool. After solidification, it reappears and ε_{zz}^{lat} exhibits a similar decrease as ε_{yy}^{lat}. A compressive strain is obtained after cooling down to room temperature (see $L_{20}+1$ at 3 s). The deposition of the next layer $L_{20}+1$ results in the same trend as the deposition of layer L_{20} but with lower amplitudes. The increase in ε_{zz}^{lat} during the laser approach corresponds to the decrease in ε_{yy}^{lat} due to the Poisson effect.

After three added layers ($L_{20}+3$) and until the end of AM processing, the maximum lattice strain reached along BD is higher than along PD. The aforementioned lattice strain evolution cycles along the two directions repeat until the end of the AM process but the magnitude of the contraction and expansion decrease with the number of added layers.

Evolution of ε_{yy}^{lat} and ε_{zz}^{lat} as a function of added layers and measurement time was also studied at heights $z = 7.4$ mm and 11 mm above the substrate (see Supplementary Figure A1). Both ε_{yy}^{lat} and ε_{zz}^{lat} evolutions at these heights were similar to the ones shown in Figure 5. However, the further the investigated position (i.e., higher z) from the substrate, the higher the maximum strain reached during each cycle and the lower the cooling rate. This is because the substrate acts as a heat sink and the regions closer to the substrate conduct away the heat faster than the regions away from the substrate.

Figure 6 shows the comparison between the experimental and simulated ε_{yy}^{lat} and ε_{zz}^{lat} lattice strain (thermal + elastic) profiles for 5 layer additions starting from the 20^{th} layer (i.e., $z =$ 4 mm); only 5 layer additions are shown for a clear interpretation. A similar comparison is shown for the 37^{th} and 55^{th} layers (i.e., $z = 7.4$ mm and $z = 11$ mm, respectively) in Supplementary Figure B2. A good qualitative agreement and a satisfactory quantitative agreement with the experimental results is obtained, even though the strain peak is overestimated. This discrepancy is mainly attributed to the fact that experimental data are averaged over the observation zone (i.e., $600 \times 500 \times 300$ µm^3 along x, y, z in the laser reference scale), while numerical data are considered at the center of mass of the elements representing a smaller volume (i.e., $600 \times 400 \times 200$ µm^3), which leads to sharper strain peaks.

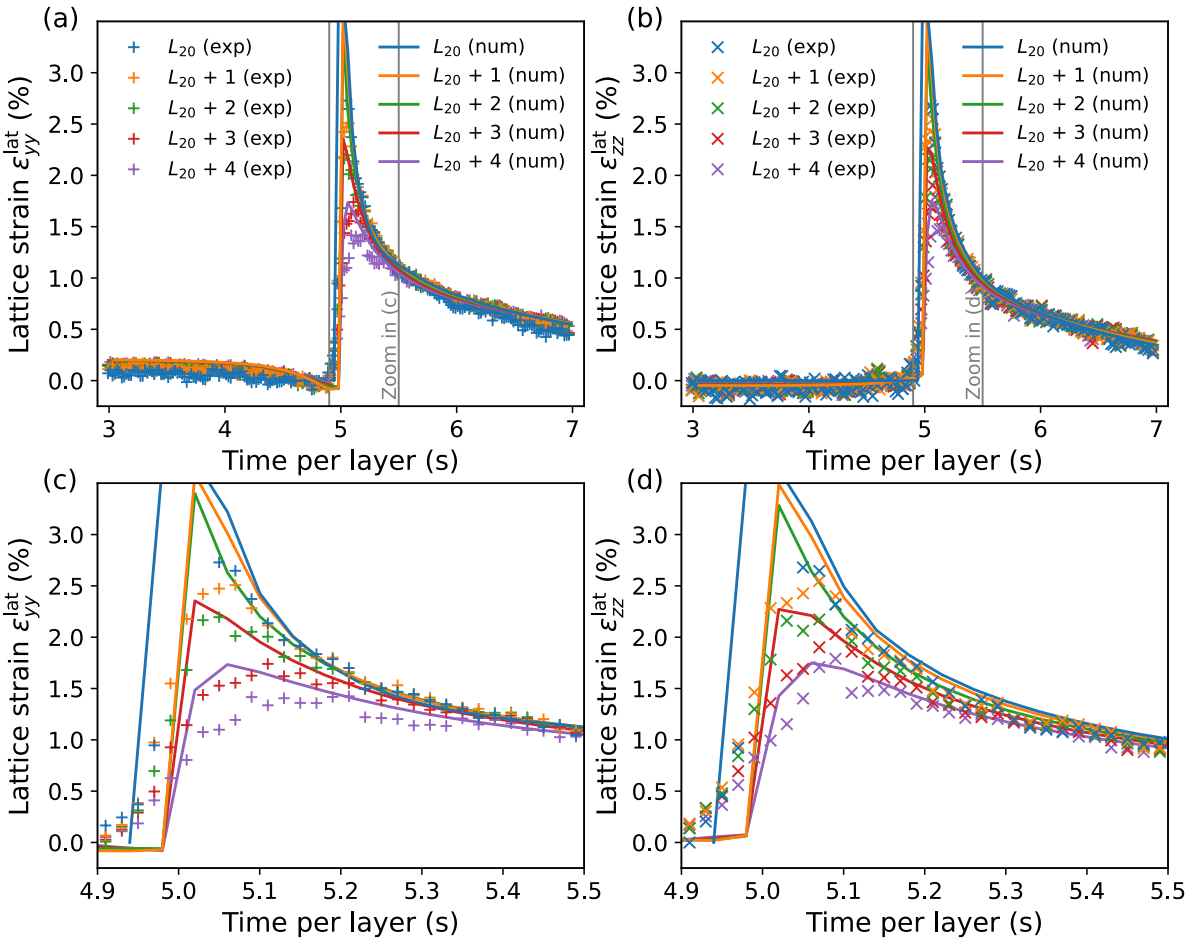

Figure 6: Computed and measured strain evolution of (a) $\varepsilon_{yy}^{\mathrm{lat}}$ (along PD) and (b) $\varepsilon_{zz}^{\mathrm{lat}}$ (along BD) at $z = 4$ mm above the substrate during the LMD process (see Figure 2 for reference to heights). Zooms of the computed and measured strain evolution during the cooling of (a) and (b) are shown respectively in (c) and (d).

Combining all these results, one can conclude that the simulations are able to capture well the experimental lattice strain evolution. It should be noted that this conclusion is limited to strains and does not include strain rates even though conclusions on errors in temperature rates are drawn in the next section. Indeed, computing time derivative from noisy experimental data is well known as an ill-posed problem needing regularization, which would make the comparison inaccurate. However, since the following section only relies on the numerical model, which is not affected by measurement noise, one can estimate more easily the error that would be introduced by neglecting elastic strains in the estimation of temperature rates from experimental data.

5 Discussion

The direct comparison between *in operando* synchrotron experiments and large-scale numerical simulation of AM process showed that the proposed numerical model not only enables to correctly capture the final residual strain but also the temperature and elastic strains during the fabrication process. It can therefore be used to estimate the error introduced by the elas-

tic strain in estimating the temperature from lattice strain. In what follows, the (error-prone) temperature directly computed from the lattice strains is:

$$T_{ii}(t) = \frac{\varepsilon_{ii}^{\mathrm{lat}}(t)}{\alpha(T(t))} + T_{\mathrm{ref}}, \qquad ii = y, z \tag{9}$$

whereas, the correct temperature is in fact $T(t) = \varepsilon^{\mathrm{th}}(t)/\alpha(T(t)) + T_{\mathrm{ref}}$, where $\varepsilon^{\mathrm{th}}(t)$ is the simulation predicted thermal strain (conventionally defined by considering the room temperature T_{ref} as a reference since the lattice strain was computed using the strain-free room temperature lattice parameter a_0 as a reference).

To quantify how the elastic strain contributes to the lattice strain (elastic + thermal), the following ratios representing the elastic contribution with respect to thermal and elastic contributions are computed:

$$\chi_{ii} = 100 \sqrt{\frac{[\varepsilon_{ii}^{\mathrm{e}}]^2}{[\varepsilon_{ii}^{\mathrm{th}}]^2 + [\varepsilon_{ii}^{\mathrm{e}}]^2}}, \qquad i = y, z \tag{10}$$

Figure 7 shows χ_{yy} and χ_{zz} profiles for 5 layer additions starting from the 20$^{\mathrm{th}}$ layer. Some fluctuations can be noticed between 5 and 5.5 s for L_{20} in Figure 7, which are due to significant variations of the elastic strain after deposition as shown in Figure B3 of the supplementary material. Before the temperature peak at $t = 5$ s the elastic strain is the major contribution in both directions PD and BD. Then the elastic strain contribution drops to only a few percent at $t = 5$ s when the temperature is at maximum (see Figure 6) and rapidly increases during cooling. Therefore, even though the elastic strain contribution is low at the maximum temperature, its rapid growth during cooling indicates that cooling rate estimated from lattice strains while neglecting the contribution of elastic strains will induce significant errors that will grow in time.

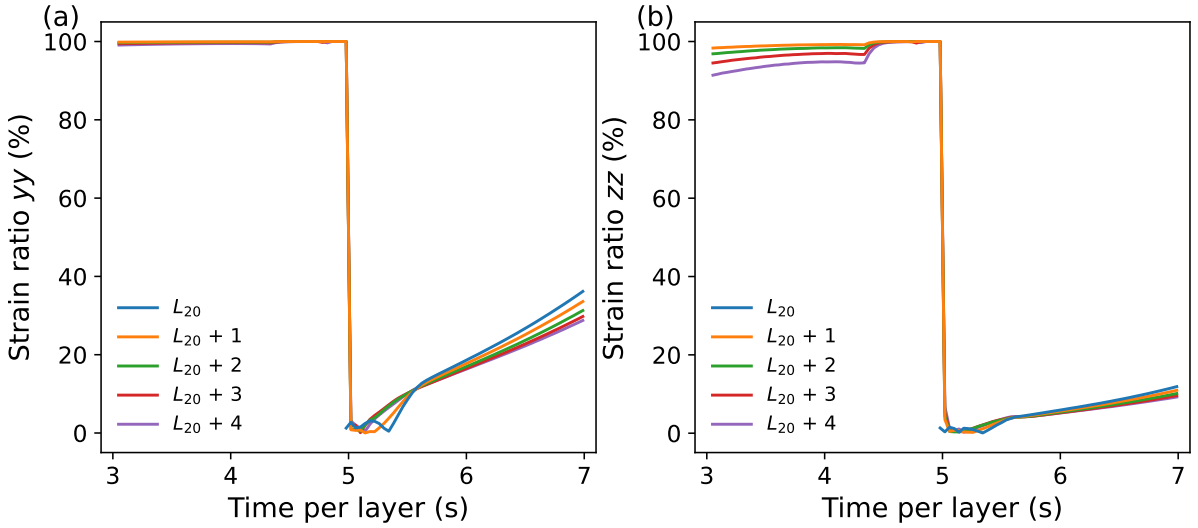

Figure 7: Evolution of ratios χ_{yy} (a) and χ_{zz} (b).

To analyse this aspect in detail, the percentage error induced in estimating temperature by not separating the contribution of elastic strains from the lattice strains:

$$\delta_{ii}(t) = 100 \left(\frac{T_{ii}(t) - T(t)}{T(t)} \right), \qquad i = y, z \tag{11}$$

and the percentage errors in estimating cooling rates:

$$\widehat{\delta}_{ii}(t) = 100 \left(\frac{\dot{T}_{ii}(t) - \dot{T}(t)}{\dot{T}(t)} \right), \qquad i = y, z \tag{12}$$

are analysed.

The temperatures T, T_{yy}, T_{zz} along with the cooling rates $\dot{T}, \dot{T}_{yy}, \dot{T}_{zz}$ are presented in Figure 8a and c and the percentage errors δ_{yy}, δ_{zz}, $\widehat{\delta}_{yy}$ and $\widehat{\delta}_{zz}$ are presented in Figure 8b and d. To facilitate interpretation, these figures are presented only for the 20^{th} layer and one cycle, but similar results are obtained for subsequent temperature cycles and other layers. Cooling rates computed are in good agreement with those expected for DED AM process [25, 26]. In addition, the evolution of the cooling rates along the two directions during the process is in good agreement with what could be expected [8]. For temperatures higher than 700 °C, δ_{yy}, δ_{zz} are both less than $\pm 3\%$. However, below 700 °C, they reach -30% for the PD and 10% for the BD as the elastic strain contribution increases during cooling (see Figure 7). As expected, the opposite behavior is observed for cooling rates. Higher errors are associated with higher cooling rates; an error as high as 27% is obtained along PD at $t \approx 5.45$ s. However, below 500 °C, the cooling rate errors remain nearly constant until the end of the added layer.

Based on these results, one may be tempted to use $\varepsilon_{zz}^{\text{lat}}$ to compute the cooling rates with the argument that a -10% error is within the experimental uncertainty and could be discounted. However, note that this error only pertains to the studied simple case, which is DED of a single-pass-per-layer thin-wall geometry using a single-phase material (negligible solid-state phase transformations). The results will differ for phase transforming materials and more complex geometries, and a simulation study will nevertheless be necessary to deduce their effects.

One may also be tempted to mitigate the errors in T and $\dot{T}$ by simply integrating the data over the full ring, i.e., $\eta \in [0°, 360°]$, as in [7,8] for instance. This approach relies on the incorrect assumption that hydrostatic elastic strain is negligible, the elastic strain along one direction (e.g., PD) is partially compensated by the Poisson effect along the perpendicular direction (e.g., BD) and the elastic strain along the other transverse direction is negligible. However, since the Poisson's ratio is approximately 0.3 in metals and alloys, this compensation is insufficient when significant elastic strains arise.

Another attempt to directly use the lattice strains obtained from the Debye-Scherrer rings without using numerical simulations to compensate the elastic contribution would be to determine whether there exists an azimuthal angle η for which at least one diagonal component of the elastic strain is negligible; this approach has been used recently to decipher temperature evolution during neutron diffraction experiments [27]. The main reason for this exercise is to determine whether one can avoid using numerical simulations to determine temperature and cooling rates from synchrotron X-ray diffraction experiments. To that end, η may be adjusted to change the coordinate system (y, z) by a rotation to obtain a secondary coordinate system denoted by y', z' so that the elastic strain components in this new system read:

$$\begin{cases} \varepsilon^{\text{e}}_{y'y'} = \varepsilon^{\text{e}}_{yy} \cos^2(\eta) + \varepsilon^{\text{e}}_{zz} \sin^2(\eta) + 2\,\varepsilon^{\text{e}}_{yz} \cos(\eta)\, \sin(\eta) \\ \varepsilon^{\text{e}}_{z'z'} = \varepsilon^{\text{e}}_{yy} \sin^2(\eta) + \varepsilon^{\text{e}}_{zz} \cos^2(\eta) - 2\,\varepsilon^{\text{e}}_{yz} \cos(\eta)\, \sin(\eta) \end{cases} \tag{13}$$

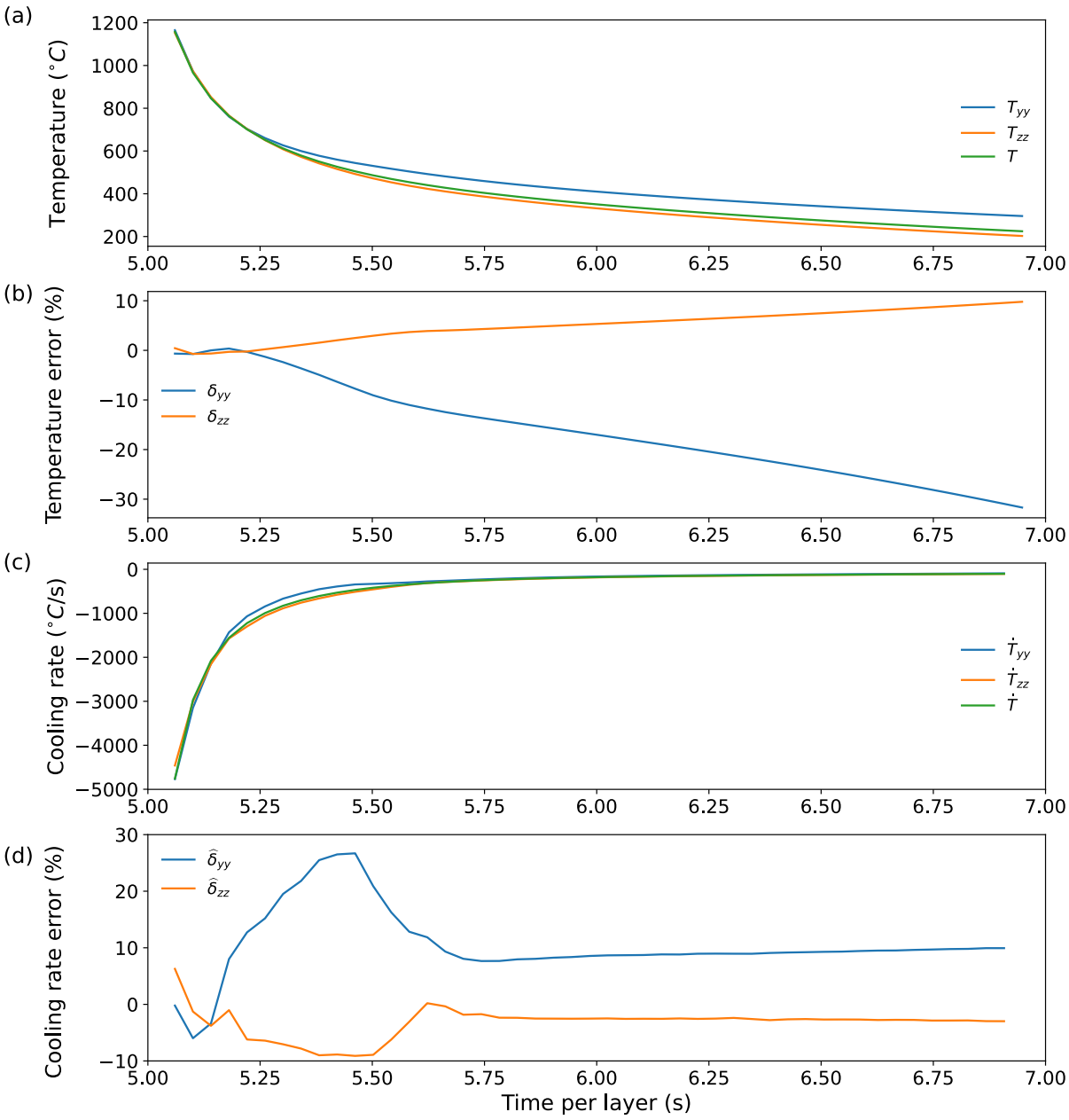

Figure 8: For the 20$^{\text{th}}$, evolution of (a) computed temperature T, estimated temperatures from lattice strains T_{yy}, T_{zz}, (b) computed cooling rate $\dot{T}$ and estimated cooling rate from lattice strains $\dot{T}_{yy}, \dot{T}_{zz}$, and corresponding evolution of (b) errors in temperature δ_{yy}, δ_{zz} and (d) errors in cooling rates $\widehat{\delta}_{yy}, \widehat{\delta}_{zz}$.

Thus, the angle η at which $\varepsilon^{\text{e}}_{y'y'} = 0$ or $\varepsilon^{\text{e}}_{z'z'} = 0$ is obtained as:

$$\begin{cases} \eta = \arctan\left(-\dfrac{\varepsilon^{\text{e}}_{yz}}{\varepsilon^{\text{e}}_{zz}} \pm \sqrt{\left(\dfrac{\varepsilon^{\text{e}}_{yz}}{\varepsilon^{\text{e}}_{zz}}\right)^2 - \dfrac{\varepsilon^{\text{e}}_{yy}}{\varepsilon^{\text{e}}_{zz}}}\right) \\ \text{if } \left(\varepsilon^{\text{e}}_{yz}\right)^2 \geq \varepsilon^{\text{e}}_{yy} \text{ and } \varepsilon^{\text{e}}_{zz} \neq 0 \end{cases} \quad \text{or} \quad \begin{cases} \eta = \arctan\left(\dfrac{\varepsilon^{\text{e}}_{yz}}{\varepsilon^{\text{e}}_{yy}} \pm \sqrt{\left(\dfrac{\varepsilon^{\text{e}}_{yz}}{\varepsilon^{\text{e}}_{yy}}\right)^2 - \dfrac{\varepsilon^{\text{e}}_{zz}}{\varepsilon^{\text{e}}_{yy}}}\right) \\ \text{if } \left(\varepsilon^{\text{e}}_{yz}\right)^2 \geq \varepsilon^{\text{e}}_{zz} \text{ and } \varepsilon^{\text{e}}_{yy} \neq 0 \end{cases} \tag{14}$$

If both $\left(\varepsilon^{\text{e}}_{yz}\right)^2 < \varepsilon^{\text{e}}_{yy}$ and $\left(\varepsilon^{\text{e}}_{yz}\right)^2 < \varepsilon^{\text{e}}_{zz}$, then one can only minimize $\left(\varepsilon^{\text{e}}_{y'y'}\right)^2$ or $(\varepsilon^{\text{e}}_{z'z'})^2$. The maximum orientation given by Equation (14) is presented in degrees in Figure 9. It is clear

that large erratic variations take place when the laser is near the observation zone (i.e., between 4.5 and 5.5 s) due to the development of shear strains (see Figure B3 in the Supplementary material). Therefore, a rule of thumb would be very difficult to establish and any such rule would be inaccurate.

Since the errors in temperature are low when the laser is near the observation zone, for the studied material, geometry, and process parameters, temperatures could be estimated from the lattice strains at $\eta \approx 60°$; note however that this may not be true in particular for materials exhibiting solid-state phase transformations. Nevertheless, estimating cooling rates will require performing simulations because of the large errors incurred when the laser is near the observation zone. Therefore, generally speaking, a fast numerical model such as the one used in this paper is well suited, and even necessary, to separate the mechanical contribution in order to correctly estimate temperature and cooling rates from synchrotron X-ray diffraction data. The need for such a model would become even more crucial when studying solid-state phase transforming materials or materials with significant amount of precipitation resulting in large internal stresses along with the stresses induced from macroscopic constraints.

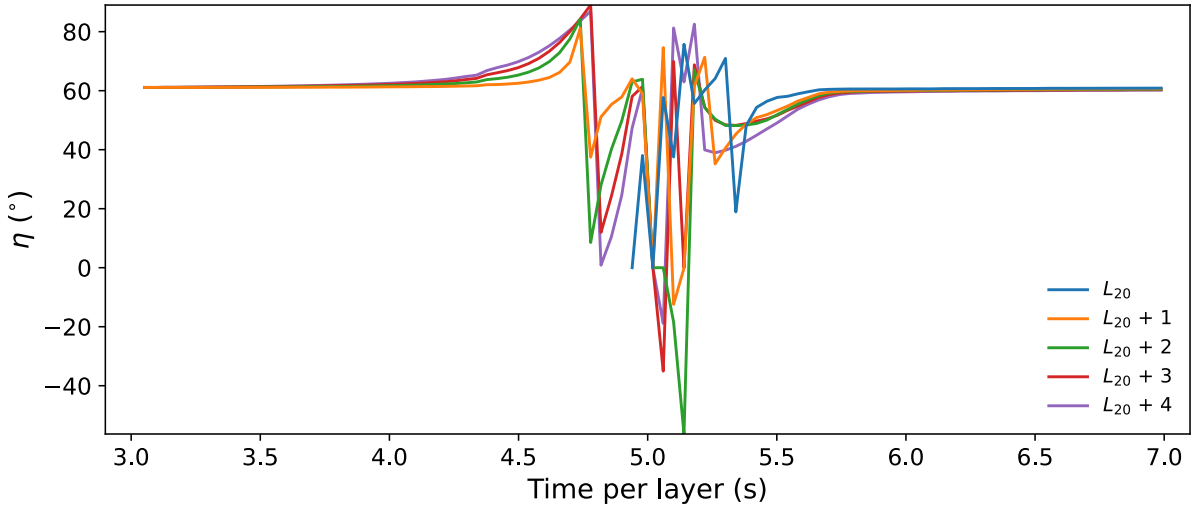

Figure 9: Maximum azimuthal angle η for which at least one diagonal component of the elastic strain tensor vanishes.

6 Conclusion

In operando synchrotron X-ray diffraction experiments were performed during AM – via the laser-based direct energy deposition (DED) process – of a 316L stainless steel (a nearly single-phase material) and used to obtain the lattice strain evolution as a function of time. In addition, the final residual elastic strain distribution in the entire sample was measured. These experimental results were used to validate a large-scale and fast numerical thermomechanical model. Good agreements were found between the experimentally measured and simulation predicted transient lattice strains and the final residual elastic strain distributions.

Based on these agreements, the model was then used to separate the thermal and elastic contributions of the lattice strain measured during *in operando* synchrotron X-ray diffraction experiments and to quantify the errors occurring in estimating the evolution of temperature and

cooling rates from experimentally measured lattice strains. A non-negligible error was obtained in estimating both the temperature (up to 30%) and the cooling rates (up to 27%) when using the experimentally measured lattice strain without removing the contribution of elastic strains due to external mechanical constraints, specifically from the bonding between the sample and the substrate. These errors are difficult to correct without complete thermomechanical computation of the elastic strains arising during the process because the error is not constant with respect to the processing time. In addition, residual strain maps show that the elastic strain is not uniform in the part (in particular, significant edge effects occur), which should be taken into account when temperatures are estimated near the sample edges or for small samples (e.g., to estimate the accumulated heat effect and possible defects).

The proposed strategy combining *in operando* synchrotron X-ray diffraction measurements and fast thermomechanical simulations enables not only to identify residual and transient strain fields, which have a significant impact on material properties and geometrical tolerances, but also to identify temperatures and heating/cooling rates, which are essential to understanding the formation of microstructures (e.g., grain morphology, grain size, phase fractions) due to solidification and subsequent evolution due to solid-state thermal cycling (intrinsic heat treatments).

Acknowledgments The authors acknowledge the support of the European Synchrotron Radiation Facility (ESRF) for beamtime access via proposal no. ME-1578 and thank Florian Russello for assistance and support in using beamline ID31. The authors thank Simon Hallais for support in conducting EBSD measurements. SG, KAA and MVU are grateful to European Research Council (ERC) for their support through the European Union's Horizon 2020 research and innovation program for project GAMMA (Grant agreement ID: 946959).

Funding This work was supported by the Horizon 2020 - EXCELLENT SCIENCE - European Research Council Starting Grant 2020 project GAMMA (Grant agreement ID: 946959).

Declaration of competing interest The authors declare no conflict of interest. The funders had no role in the design of the study, collection, analyses, and interpretation of data in the writing of the manuscript, or in the decision to publish the results.

Data availability Data will be made available on request. Open access to synchrotron experimental raw data will be available on December 2024, see https://doi.org/10.15151/ESRF-ES-611485530

References

[1] Cody S. Lough, Xin Wang, Christopher C. Smith, Robert G. Landers, Douglas A. Bristow, James A. Drallmeier, Ben Brown, and Edward C. Kinzel. Correlation of SWIR imaging with LPBF 304L stainless steel part properties. Additive Manufacturing, 35:101359, 2020.

[2] Sarah K. Everton, Matthias Hirsch, Petros Stravroulakis, Richard K. Leach, and Adam T. Clare. Review of in-situ process monitoring and in-situ metrology for metal additive manufacturing. Materials & Design, 95:431–445, 2016.

[3] Daniel Weisz-Patrault. Fast simulation of temperature and phase transitions in directed energy deposition additive manufacturing. Additive Manufacturing, 31:100990, 2020.

[4] Wei Chen, Lianyong Xu, Yongdian Han, Lei Zhao, and Hongyang Jing. Control of residual stress in metal additive manufacturing by low-temperature solid-state phase transformation: An experimental and numerical study. Additive Manufacturing, 42:102016, 2021.

[5] Daniel Weisz-Patrault, Pierre Margerit, and Andrei Constantinescu. Residual stresses in thin walled-structures manufactured by directed energy deposition: In-situ measurements, fast thermo-mechanical simulation and buckling. Additive Manufacturing, 56:102903, 2022.

[6] Samy Hocine, Helena Van Swygenhoven, Steven Van Petegem, Cynthia Sin Ting Chang, Tuerdi Maimaitiyili, Gemma Tinti, Dario Ferreira Sanchez, Daniel Grolimund, and Nicola Casati. Operando X-ray diffraction during laser 3D printing. Materials Today, 34:30–40, 2020.

[7] Yunhui Chen, Samuel J Clark, David M Collins, Sebastian Marussi, Simon A Hunt, Danielle M Fenech, Thomas Connolley, Robert C Atwood, Oxana V Magdysyuk, Gavin J Baxter, et al. Correlative synchrotron X-ray imaging and diffraction of directed energy deposition additive manufacturing. Acta Materialia, 209:116777, 2021.

[8] Antonio Carlos de F. Silveira, Rainer Fechte-Heinen, and Jérémy Epp. Microstructure evolution during laser-directed energy deposition of tool steel by in situ synchrotron X-ray diffraction. Additive Manufacturing, 63:103408, 2023.

[9] Ming Chen, Marco Simonelli, Steven Van Petegem, Yau Yau Tse, Cynthia Sin Ting Chang, Malgorzata Grazyna Makowska, Dario Ferreira Sanchez, and Helena Moens-Van Swygenhoven. A quantitative study of thermal cycling along the build direction of Ti-6Al-4V produced by laser powder bed fusion. Materials Design, 225:111458, 2023.

[10] Hans-Henrik König, Niklas Holländer Pettersson, A Durga, Steven Van Petegem, Daniel Grolimund, Andrew Chihpin Chuang, Qilin Guo, Lianyi Chen, Christos Oikonomou, Fan Zhang, et al. Solidification modes during additive manufacturing of steel revealed by high-speed X-ray diffraction. Acta Materialia, page 118713, 2023.

[11] Pooriya Gh Ghanbari, Patrik Markovic, Steven Van Petegem, Malgorzata Grazyna Makowska, Rafal Wrobel, Thomas Mayer, Christian Leinenbach, Edoardo Mazza, and Ehsan Hosseini. A close look at temperature profiles during laser powder bed fusion using operando X-ray diffraction and finite element simulations. Additive Manufacturing Letters, page 100150, 2023.

[12] Steve Gaudez, Kouider Abdellah Abdesselam, Hakim Gharbi, Zoltan Hegedüs, Ulrich Lienert, Wolfgang Pantleon, and Manas Vijay Upadhyay. High-resolution reciprocal space mapping reveals dislocation structure evolution during 3D printing. Additive Manufacturing, page 103602, 2023.

[13] Daniel Weisz-Patrault, Sofia Sakout, and Alain Ehrlacher. Fast simulation of temperature and grain growth in directed energy deposition additive manufacturing. In 14th WCCM-ECCOMAS Congress. Scipedia, 2021.

[14] Alexander Edwards, Daniel Weisz-Patrault, and Eric Charkaluk. Analysis and fast modelling of microstructures in duplex stainless steel formed by directed energy deposition additive manufacturing. Additive Manufacturing, 61:103300, 2023.

[15] Dieter Bäuerle. Laser processing and chemistry. Springer Science & Business Media, 2013.

[16] High temperature characteristics of stainless steels. Technical report, A Designers' Handbook Series No. 9004. American Iron and Steel Institute, 2011.

[17] Seung Seok Lee, Un-Sig Min, Bongyoung Ahn, and Seung Hyun Yoo. Elastic constants determination of thin cold-rolled stainless steels by dynamic elastic modulus measurements. Journal of materials science, 33(3):687–692, 1998.

[18] Pierre Margerit, Daniel Weisz-Patrault, Krishnaswamy Ravi-Chandar, and Andrei Constantinescu. Tensile and ductile fracture properties of as-printed 316L stainless steel thin walls obtained by directed energy deposition. Additive Manufacturing, 37:101664, 2021.

[19] Yanis Balit, Eric Charkaluk, and Andrei Constantinescu. Digital image correlation for microstructural analysis of deformation pattern in additively manufactured 316L thin walls. Additive Manufacturing, 31:100862, 2020.

[20] Choong S Kim. Thermophysical properties of stainless steels. Technical report, Argonne National Lab., Ill.(USA), 1975.

[21] P Mercelis and J-P Kruth. Residual stresses in selective laser sintering and selective laser melting. Rapid prototyping journal, 2006.

[22] Felix Schmeiser, Erwin Krohmer, Norbert Schell, Eckart Uhlmann, and Walter Reimers. Experimental observation of stress formation during selective laser melting using in situ X-ray diffraction. Additive Manufacturing, 32:101028, 2020.

[23] Seunghee A Oh, Rachel E Lim, Joseph W Aroh, Andrew C Chuang, Benjamin J Gould, Behnam Amin-Ahmadi, Joel V Bernier, Tao Sun, P Chris Pistorius, Robert M Suter, et al. High speed synchrotron X-ray diffraction experiments resolve microstructure and phase transformation in laser processed Ti-6Al-4V. Materials Research Letters, 9(10):429–436, 2021.

[24] Tuhin Mukherjee, W Zhang, and Tarasankar DebRoy. An improved prediction of residual stresses and distortion in additive manufacturing. Computational Materials Science, 126:360–372, 2017.

[25] W Hofmeister and M Griffith. Solidification in direct metal deposition by lens processing. Jom, 53(9):30–34, 2001.

[26] David Svetlizky, Mitun Das, Baolong Zheng, Alexandra L Vyatskikh, Susmita Bose, Amit Bandyopadhyay, Julie M Schoenung, Enrique J Lavernia, and Noam Eliaz. Directed energy deposition (DED) additive manufacturing: Physical characteristics, defects, challenges and applications. Materials Today, 49:271–295, 2021.

[27] Alex Plotkowski, Kyle Saleeby, Christopher M Fancher, James Haley, Guru Madireddy, Ke An, Rangasayee Kannan, Thomas Feldhausen, Youseb Lee, Dunji Yu, et al. Operando

neutron diffraction reveals mechanisms for controlled strain evolution in 3d printing. Nature Communications, 14(1):4950, 2023.